Nanocarbon-Based Photovoltaics

Marco Bernardi,[†,⊥] Jessica Lohrman,[‡,⊥] Priyank V. Kumar,[†] Alec Kirkeminde,[‡] Nicola Ferralis,[†] Jeffrey C. Grossman,[†,*] and Shenqiang Ren[‡,*]

[†]Department of Materials Science and Engineering, Massachusetts Institute of Technology, 77 Massachusetts Avenue, Cambridge, Massachusetts 02139-4307, United States and [‡]Department of Chemistry, University of Kansas, 1251 Wescoe Hall Drive, Lawrence, Kansas 66045, United States. [⊥]These authors contributed equally to this work.

ABSTRACT

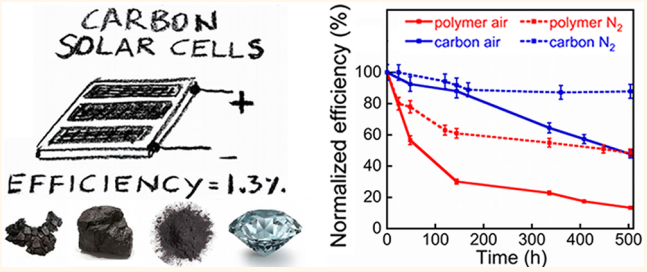

Carbon materials are excellent candidates for photovoltaic solar cells: they are Earth-abundant, possess high optical absorption, and maintain superior thermal and photostability. Here we report on solar cells with active layers made solely of carbon nanomaterials that present the same advantages of conjugated polymer-based solar cells, namely, solution processable, potentially flexible, and chemically tunable, but with increased photostability and the possibility to revert photodegradation. The device active layer composition is optimized using *ab initio* density functional theory calculations to predict type-II band alignment and Schottky barrier formation. The best device fabricated is composed of $PC_{70}BM$ fullerene, semiconducting single-walled carbon nanotubes, and reduced graphene oxide. This active-layer composition achieves a power conversion efficiency of 1.3%—a record for solar cells based on carbon as the active material—and we calculate efficiency limits of up to 13% for the devices fabricated in this work, comparable to those predicted for polymer solar cells employing PCBM as the acceptor. There is great promise for improving carbon-based solar cells considering the novelty of this type of device, the high photostability, and the availability of a large number of carbon materials with yet untapped potential for photovoltaics. Our results indicate a new strategy for efficient carbon-based, solution-processable, thin film, photostable solar cells.

KEYWORDS: photovoltaics · carbon · photodegradation · *ab initio* materials design

The energy generated from solar photovoltaics (PV) amounts to less than 1% of the total worldwide energy usage at present, for the main reason that producing a kWh of energy from PV panels costs significantly more than burning fossil fuels.[1] Despite an impressive learning curve for PV technology that has brought Si solar cells ever closer to the Schockley–Queisser efficiency limit of ~30%,[1−3] grid-parity PV remains an enormous challenge in most parts of the world. As possible alternatives to inorganic semiconductor PV technology, a number of new materials have emerged: for example, solar cells based on conjugated polymers,[4,5] small molecules,[6] and colloidal nanocrystals[7] are justified by the possibility of utilizing thin film (<1 μm) materials with high optical absorption, as well as using lightweight flexible substrates, printable organic inks, and low temperature and ambient pressure fabrication, enabling reduced device and balance of system costs.[2,4] The ability to use chemical vapor or solution deposition processing is particularly exciting since products such as paper, textiles, automobiles, and building materials could be coated with PV devices thus making solar cells ubiquitous.

Carbon, one of the few elements known since antiquity, holds remarkable potential as an inexpensive material for solar cells.[8] Not only is it abundant in the Earth's crust (~0.2 wt %),[9] but it can also be found in nature in several forms such as graphite, diamond, and coal, and it is widely used technologically with a record production among other elements of 9 Gt/year.[9] Nanostructured carbon allotropes have been intensively investigated in the past two decades, including single−walled carbon nanotubes (SWCNT),[10,11] fullerenes,[12] graphene,[13,14] and their chemical derivatives. These materials hold record values for physical properties important for PV such as carrier mobility and optical absorption, and they are appealing for PV as they can be dissolved in organic solvents to deposit thin solar cell active layers from solution. Other carbon allotropes such as amorphous carbon, nanodiamonds, and graphene can be deposited in thin film form on flexible substrates using chemical vapor deposition.[8]

While there has been intense focus on the use of carbon nanomaterials in areas such as

* Address correspondence to jcg@mit.edu, shenqiang@ku.edu.

Received for review June 28, 2012 and accepted September 6, 2012.

Published online September 06, 2012
10.1021/nn302893p

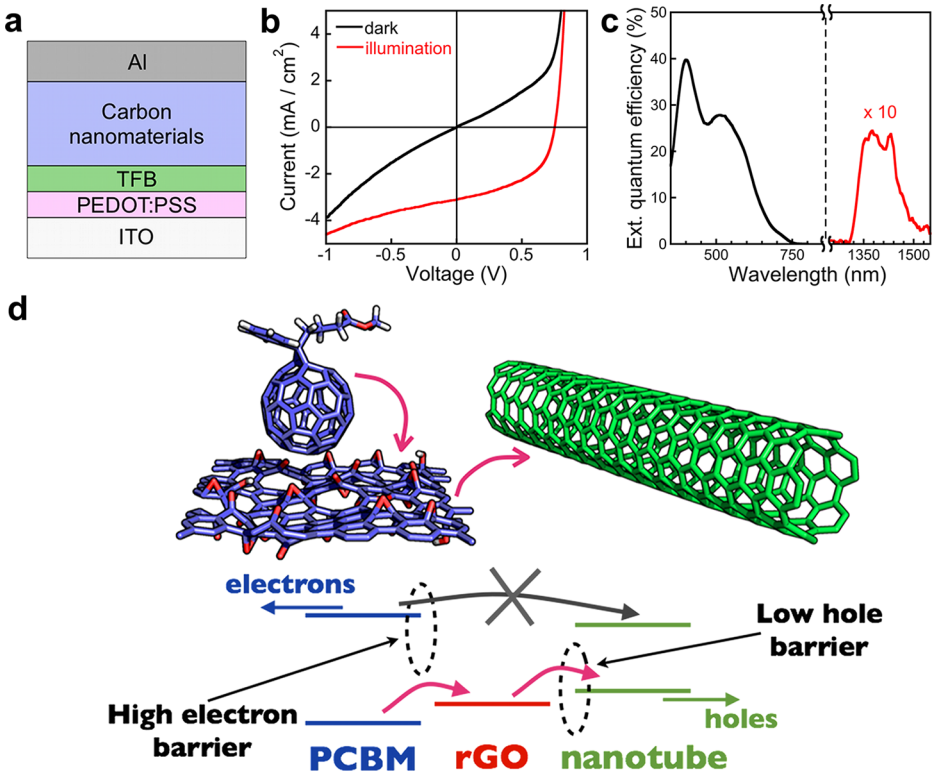

Figure 1. (a) Structure of carbon solar cells prepared in this work. Al is the top contact, TFB and PEDOT:PSS are respectively an electron-blocking and a hole-conducting layer deposited on top of the ITO bottom contact. For the best-efficiency device, the active layer, denoted by "carbon nanomaterials", contains a blend of rGO, $PC_{70}BM$, and s-SWCNT with a diameter of 1.2−1.7 nm. (b) Current−voltage curves in the dark and under simulated sunlight illumination (1 Sun, AM1.5 spectrum) of the best-efficiency device studied in this work. (c) External quantum efficiency of the best-efficiency device, showing contributions from the $PC_{70}BM$ at visible wavelengths (black curve), and from the nanotube S_{11} optical transitions centered at 1400 nm in the infrared (red line, multiplied by 10 for clarity). (d) Interface of PCBM/rGO sheet/s-SWCNT, representing schematically the active layer components of the best-efficiency device. The pink arrows trace the transfer cascade of hole carriers photogenerated within PCBM, selectively injected to rGO due to a large Schottky barrier for electrons, and then transferred to s-SWCNT. The schematic band diagram below shows the same process together with the highest occupied molecular orbital (HOMO) and lowest unoccupied molecular orbital (LUMO) energies for PCBM and carbon nanotubes, and the Fermi energy or rGO. The crossed gray arrow indicates the absence of electron flow from PCBM to s-SWCNT.

electronics and photonics,[15] the potential of carbon as the active layer material in PV is still largely unexplored. In PV, carbon materials have been mainly used as acceptors in polymer-based solar cells[4−6,8,16] or as transparent electrodes, buffer layers, interfacial layers, and interconnects,[8] and only recently as the main active layer components in polymer−free solar cells.[17−21] In these works, C_{60} or C_{70} fullerenes were evaporated to form bilayer devices in combination with either SWCNT[17−19] or a composite of SWCNT/rGO/fullerene deposited from aqueous solution.[20,21] For such polymer-free, carbon-based devices, the highest reported efficiencies to date are 0.21% for active layers based on C_{60} (ref 20) and 0.85% for devices employing C_{70} (ref 21).

RESULTS

Figure 1a shows a schematic of the carbon-based solar cells fabricated in this work, achieving a maximum efficiency of 1.3%. The active layer is entirely deposited from solution and is composed of semiconducting SWCNT (s-SWCNT), the fullerene derivative PCBM,[4] and reduced graphene oxide (rGO),[22] forming a bulk-heterojunction morphology[4] made entirely of carbon nanomaterials. The active layer does not contain other constituents such as conjugated polymers or small molecules, and the atomic carbon concentration in the active layer is as high as 80−90 atom %, *versus* carbon concentrations of 40−50 atom % for typical solar cells based on P3HT polymer. The carbon material combinations considered here include small diameter s-SWCNT (diameter $d = 0.75-1.2$ nm) or large diameter s-SWCNT ($d > 1.2$ nm), together with either $PC_{60}BM$ or $PC_{70}BM$ (the latter is used for enhanced optical absorption in the visible),[23] and with or without the addition of rGO. Optimized carrier extraction is achieved by using hole transport and electron blocking layers in conjunction with transparent indium tin oxide (ITO) and Al contacts (see Methods).

The best-efficiency device has a composition of $PC_{70}BM$ (95 wt %)/rGO (2 wt %)/s-SWCNT (3 wt %, $d >$ 1.2 nm); it achieves an efficiency of 1.3%, deriving from a short-circuit current (J_{sc}) of 3.1 mA/cm^2, an open circuit voltage (V_{oc}) of 0.75 V, and a fill factor (FF) of 0.55

TABLE 1. Several Tested Active Layer Compositions and the Corresponding J_{SC}, V_{OC}, FF, and Power Conversion Efficiency for the Best-Efficiency Device Prepared for Each Material Combination[a]

composition (wt %)	J_{sc} (mA/cm^2)	V_{oc} (V)	FF	efficiency (%)
$PC_{60}BM$ (90−99%)/D1-s-SWCNT (1−10%)	1.2	0.6	0.24	0.17
$PC_{70}BM$ (90−99%)/D1-s-SWCNT (1−10%) (*)	2.2	0.55	0.35	0.42
$PC_{60}BM$ (90−99%)/D2-s-SWCNT (1−10%)	0	0	0	0
$PC_{70}BM$ (90−99%)/D2-s-SWCNT (1−10%)	0	0	0	0
$PC_{70}BM$ (98%)/rGO control sample	0.17	0.21	0.24	0.009
$PC_{60}BM$ (88−97%)/D1-s-SWCNT (1−10%)/rGO (∼2%) (*)	0.12	0.8	0.43	0.042
$PC_{60}BM$ (88−97%)/D2-s-SWCNT (1−10%)/rGO (∼2%)	1.39	0.73	0.61	0.62
$PC_{70}BM$ (88−97%)/D2-s-SWCNT (1−10%)/rGO (∼2%) (**)	3.1	0.75	0.55	1.3

[a] Over 10 devices of each kind were fabricated and tested, yielding a 5% standard deviation on the efficiency. D1-s-SWCNT refers to small diameter nanotubes (d of 0.75−1.2 nm) and D2-s-SWCNT refers to large diameter nanotubes (d > 1.2 nm) used in this work. The symbol (∗) indicates that EQE curves for these devices are available in Supporting Information, Figure S2. The symbol (∗∗) in the last row refers to the best-efficiency device prepared in this work and shown in Figure 1, achieving an efficiency of 1.3%.

(Figure 1b and Table 1). For comparison, a control sample constituted only of $PC_{70}BM$/rGO (Table 1) without nanotubes showed an efficiency of 0.009%, more than 2 orders of magnitude lower. This indicates the key role of s-SWCNT as a hole transport material as well as infrared absorber. The external quantum efficiency (EQE, Figure 1c) shows contributions from photon absorption occurring both in the s-SWCNT donor and in the $PC_{70}BM$ acceptor. The EQE in the visible derives from optical transitions in the $PC_{70}BM$, with a main peak at ∼400 nm and a shoulder peak at 550 nm.[23] The EQE peak in the infrared centered at 1400 nm is due to the S_{11} optical transitions in s-SWCNT with 1.2−1.7 nm diameter, as found in our previous work using the same nanotubes in a polymer-based device.[16] The PV operating mechanism involves a photogenerated hole carrier cascade from $PC_{70}BM$ to rGO and then to s-SWCNT (Figure 1d), as explained below. We have fabricated and tested a large set of devices with different ratios and types of PCBM, s-SWCNT and rGO; their performance is summarized in Table 1, and additional EQE curves for some devices are reported in Supporting Information, Figure S2.

We employed first-principles calculations (Figure 2 and Supporting Information, Figure S1) to design the optimal combination of carbon nanomaterials used to prepare the device shown in Figure 1. For a bulk heterojunction (BHJ) solar cell containing SWCNT in the active layer, it is crucial to avoid the presence of metallic nanotubes to avoid short-circuiting the electrodes[16,24] and exciton quenching.[18] For this reason, only semiconducting nanotubes are used in this work. For a two-component active layer made of s-SWCNT and PCBM, the band alignment (calculated here using density functional theory,[25,26] DFT; see Methods) depends critically on the nanotube diameter d. The HOMO and LUMO level energy offsets (ΔE_V and ΔE_C, respectively, Figure 2a) vary not only due to the nanotube work function and band gap variation with d, but also due to a charge redistribution causing the formation of an interface dipole, thus requiring *ab initio* calculations of the full interface to compute the band offsets. For a two-phase active layer of s-SWCNT/PCBM, a type-II alignment is ideal for PV operation as it allows the s-SWCNT to work as the donor and the PCBM to work as the acceptor in a BHJ solar cell,[4] thus leading to favorable dissociation of excitons photogenerated in either material. We analyze the case of $PC_{60}BM$ for convenience (due to its higher symmetry, the interfaces with s-SWCNT can be more straightforwardly defined), though $PC_{70}BM$ yields the same trends both in the calculations and in the experiments due to its very similar electronic structure to $PC_{60}BM$.

For all nanotubes studied here (d = 0.75−1.7 nm), the nanotube HOMO level is found to be higher in energy than the HOMO level of PCBM (*i.e.*, $\Delta E_V > 0$ in Figure 2a), and thus the HOMO orbital of the interface is localized on s-SWCNT. For a small d between 0.75 and 1.2 nm, positive conduction band offsets are found, as confirmed by the interface LUMO orbitals localized on the nanotube (Figure 2a). A type-II alignment favorable for PV operation is thus predicted for nanotubes with diameters of 0.75−1.2 nm. In particular, for the (6,5) nanotube (d = 0.75 nm) constituting up to 50% of the small diameter s-SWCNT sample used in our experiments, the alignment is predicted to be type II with $\Delta E_C \approx 0.2$ eV, as shown in Figure 1a; this is consistent with a rigid band alignment model yielding $\Delta E_C = 0.6$ eV for the (6,5) nanotube/C_{60} interface as obtained in ref 19, given the 0.4−0.5 eV difference between the electron affinities of PCBM and C_{60}.[27] We also observe that the small-diameter (10,0) nanotube ($d \approx 0.8$ nm) is an outlier and yields type-I alignment within our DFT calculation. However, even if the (10,0) chirality does not contribute to the photocurrent in our sample, this is irrelevant given the large number of chiralities in a s-SWCNT sample with diameter of 0.75−1.2 nm. For large diameter nanotubes with d > 1.2 nm, the LUMO levels of PCBM and s-SWCNT are nearly degenerate, and the LUMO orbital is seen to extend across the interface (Figure 2a), thus yielding type-I alignment.

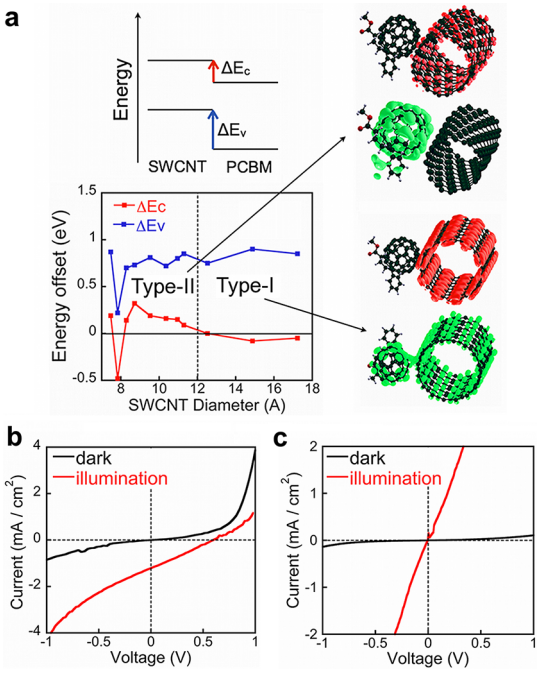

Figure 2. (a) Energy offsets of HOMO (ΔE_V) and LUMO (ΔE_C) levels for PCBM/s-SWCNT interfaces, calculated using DFT and shown as a function of nanotube diameter. The offsets are referenced to the HOMO and LUMO levels of the acceptor, as shown above the plot. The two diameter ranges with type-I and type-II alignment are indicated and delimited by a vertical dashed line at d = 1.2 nm. The smallest diameter shown is the (6,5) nanotube, with type-II alignment and $\Delta E_C \approx 0.2$ eV. Also shown are charge density plots for the HOMO (in red) and LUMO (in green) orbitals for type-II and type-I cases, as indicated by the arrows. The band offset predictions are confirmed by measurements of the current–voltage characteristics, shown in panel b for our fabricated devices with nanotube diameter of 0.75–1.2 nm, and in panel c for devices with nanotubes with d > 1.2 nm. The same trends are found if $PC_{70}BM$ is used instead of $PC_{60}BM$ (see Table 1).

On the basis of these trends, a rectifying behavior favorable for PV operation is expected for a BHJ device employing PCBM and s-SWCNT with $d \approx 0.75$–1.2 nm in the active layer, while ohmic behavior and no PV effect are expected in a similar device employing s-SWCNT with d > 1.2 nm.

We verified experimentally these trends by preparing BHJ solar cells using PCBM and diameter-sorted s-SWCNT with both diameter ranges, and found excellent agreement with the predictions from our DFT calculations, both for $PC_{60}BM$ and $PC_{70}BM$ (Figure 2b,c). In this first part of our study, we thus conclude that large diameter s-SWCNT in combination with PCBM cannot provide PV conversion, while a suitable carbon-based solar cell can be prepared using a two-phase active layer of PCBM and s-SWCNT with $d \approx$ 0.75–1.2 nm. However, in the small diameter s-SWCNT/PCBM devices we fabricated, the high van der Waals attractive force between small-diameter nanotubes caused extensive nanotube bundling and poor overall morphology (Figure 3a), and we were only

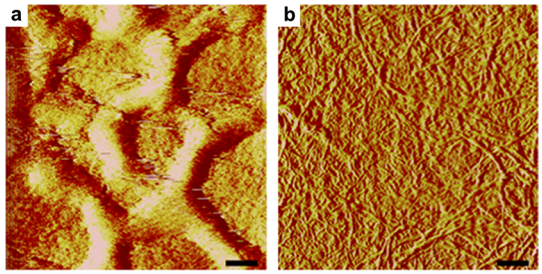

Figure 3. (a) AFM phase image of a device with active layer of PCBM/s-SWCNT with $d \approx$ 0.75–1.2 nm, showing the presence of nanotube bundles of up to 200 nm width. (b) Same image as in panel a but for a device made with larger diameter nanotubes (d >1.2 nm), where the active layer components form a well-blended morphology without the formation of large nanotube bundles. Similar morphologies are found upon addition of rGO in both cases. The scale bar is 200 nm in both images.

able to achieve a maximum efficiency of ~0.4% using either $PC_{60}BM$ or $PC_{70}BM$ in combination with small-diameter nanotubes (Table 1).

We obtained a much smoother active layer morphology for nanotubes of larger diameter d > 1.2 nm blended with PCBM (Figure 3b); however, as mentioned before, these blends are unsuitable for PV operation due to type-I alignment. In order to take advantage of the favorable morphology of this blend, we added rGO as a third material phase that can induce exciton dissociation at the interface with PCBM or s-SWCNT. We found that this three-phase combination of PCBM/rGO/s-SWCNT with d > 1.2 nm can simultaneously achieve favorable morphology and exciton dissociation constitutes the active layer material of our best-efficiency device shown in Figure 1.

To understand the role of rGO in enabling exciton dissociation in such three-phase system shown in Figure 1, we computed the electronic structure of rGO sheets with disordered oxygen-containing groups and O concentrations in the range of 10–20 atom % (as employed here experimentally), as well as of rGO/s-SWCNT and rGO/PCBM interfaces. In all cases considered here, rGO is found to be overall metallic, though due to the presence of local energy gaps it should be regarded as a highly disordered amorphous semiconductor, consistent with previous experimental observations.[22] Our calculations for the rGO/PCBM and rGO/s-SWCNT interfaces predict the formation of n-type Schottky barriers larger than 1 eV for electrons to be transferred from PCBM to rGO (Supporting Information, Figure S1), and low p-type barriers for holes to be transferred from PCBM to rGO. Thus the transfer of holes from PCBM (with ionization energy of ~6.0 eV) to rGO (for which we calculated a work function of 5.1–5.3 eV for O concentrations of 10–20 atom %) is both kinetically and energetically favorable. On the other hand, the transfer of electrons photogenerated within PCBM is kinetically hindered by large Schottky barriers. We also found small (~0.2 eV) p-type

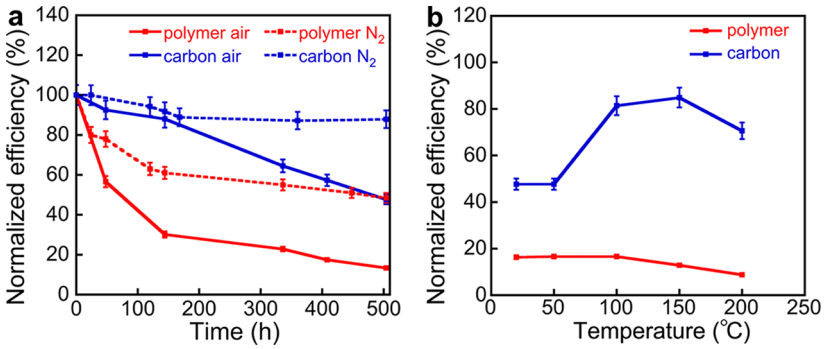

Figure 4. (a) Aging in air and in nitrogen of nonencapsulated solar cells, quantified by the time evolution of the percent fraction of the initial efficiency for the given device. A P3HT polymer/PCBM solar cell (referred to as "polymer" in figure) is compared with a SWCNT/PCBM/rGO solar cell ("carbon" curves in figure). A standard deviation of ~5% is shown for all the efficiency values reported here, based on a statistical sample of ~10 devices tested under the same conditions for each case. (b) Thermal annealing at different temperatures of devices previously aged in air for 500 h. An optimal annealing temperature of 150 °C allows a partial reversal of the photodegradation of carbon-based devices, by restoring the efficiency up to 85% of the initial value. The same reversibility is not observed in a polymer-based device.

Schottky barriers for holes to be transferred from rGO to s-SWCNT, and ionization energies of ~4.8 eV for s-SWCNT with $d > 1.2$ nm. On the basis of these calculations, an operating mechanism for the best-efficiency device is suggested in Figure 1d, whereby holes photogenerated in PCBM, which is responsible for most of the photocurrent (see Figure 1c), are selectively transferred to rGO due the large Schottky barrier for electrons at this interface, and then to s-SWCNT due to a low hole barrier. The energetics of this process are favorable due to decreasing hole energy along this path, and due to the small kinetic barriers encountered as predicted by our calculations. A similar carrier−transfer cascade mechanism involving rGO interfaces has been recently suggested in the literature in a different system.[28] We note that in contrast the addition of rGO has a negative impact on PCBM/s-SWCNT devices with small diameter nanotubes (Table 1 and Supporting Information, Figure S2), due to the poor active layer morphology and to the fact that exciton dissociation is already possible in these devices in the absence of rGO because of type-II alignment.

Next, we describe the photodegradation (PD) behavior of carbon-based solar cells prepared in this work. PD is an open technological problem in polymer-based solar cells, requiring tight encapsulation and leading to device failure. Recent studies have significantly contributed to the understanding of PD patterns in polymer-based solar cells, by showing the presence of a burn-in process leading to the rapid initial degradation of encapsulated devices.[29]

In Figure 4a we compare the PD of PCBM/s-SWCNT/rGO carbon-based solar cells with that of a polymer-based P3HT/PCBM device[4] prepared and tested at the same time, under natural illumination and exposed to ambient environment *without encapsulation*. The P3HT/PCBM device shows a burn-in process leading to a rapid efficiency drop in the first 100 h, while the carbon-based device shows a gradual efficiency decrease without burn-in, contributed in equal measure from a decrease in J_{sc} and V_{oc} (Supporting Information, Figure S3). After aging both devices for 500 h, the efficiency of the polymer-based device dropped to ~15% of the initial value *versus* a much lower decrease to ~50% of the initial value for the carbon-based solar cell. The fact that the burn-in process only appears in devices where the polymer is present is in agreement with is in agreement with ref 29, where the rapid efficiency decrease is attributed to chemical changes in the polymer.

If oxygen and moisture are eliminated by carrying out the same aging test in a nitrogen glovebox (Figure 4a), the efficiency only decreases by 5−10% over 500 h for the carbon-based solar cell (both with and without rGO), *versus* a decrease by as much as 50% for the polymer based device. The significantly lower PD rate for carbon-based devices in a nitrogen environment compared to air suggests that oxidative processes due to the presence of PCBM are responsible for the PD in air seen in Figure 4a, consistent with recent PD studies of PCBM.[30] The residual PD for the polymer-based solar cell in nitrogen suggests on the other hand that polymer PD is partially contributed by optical excitation processes independent of the presence of oxygen.

Finally, we show in Figure 4b an effect unique to carbon-based PV devices: upon thermal heating in vacuum for 10 min of a PCBM/s-SWCNT/rGO solar cell previously aged for 500 h in air, the efficiency can be restored to 85% of its initial value if the proper annealing temperature is chosen, likely due to the partial reversibility of the PD oxidative processes. The same effect is not observed for a polymer-based solar cell (Figure 4b).

DISCUSSION

There is significant potential to increase the efficiency of carbon-based solar cells beyond the 1.3% value reported here. The theoretical efficiency limit[31] of such devices depends on the optical gap of the

materials present in the active layer, as well as on the maximum voltage achievable and on carrier and exciton transport. For the s-SWCNT/PCBM fabricated in this work, we estimate efficiency limits of 9% and 13%, respectively, for nanotube diameters of 1.2−1.7 nm and 0.75−1.2 nm, as derived in the analysis below.

The main active layer constituent (~90 wt %) in our study is $PC_{60}BM$ (or $PC_{70}BM$), which contributes to most of the photocurrent and quantum efficiency as shown in Figure 1c. This also implies that absorption is limited to photons with energy above the optical gap of PCBM—apart from a small contribution from s-SWCNT absorption in the infrared, neglected here—and we can thus approximate the maximum short−circuit current J_{sc} as

$$J_{sc} = e \int_{E_{opt}}^{\infty} J_{ph}(E)\, dE$$

where E_{opt} is the optical gap of PCBM (~1.8 eV), J_{ph} is the incident solar photon flux for the AM 1.5 spectrum (ref 32), E is the incident photon energy, and EQE = 100% is assumed. For the case of a PCBM absorber, this yields an upper limit for J_{sc} of 19.6 mA/cm^2.

For an excitonic solar cell with exciton dissociation occurring at donor−acceptor heterojunctions, the maximum V_{oc} can be approximated by the interface energy gap, namely the energy difference between the interface HOMO level (contributed here by the SWCNT donor) and the interface LUMO level from the PCBM acceptor. For small values of ΔE_C, for example, ~0.2 eV as found here in Figure 1a, the maximum interface energy gap is approximately equal to the s-SWCNT energy gap, here taken as the average for the considered diameter range. This leads to limits in the V_{oc} values of approximately 1.0 V for nanotube diameters of 0.75−1.2 nm and 0.7 V for nanotube diameters of 1.2−1.7 nm, in agreement with the V_{oc} found in this work. A fill factor (FF) value of 0.65 can be assumed for a device with minor internal resistances, as done in estimating efficiency limits for polymer solar cells;[33] this is not far from the 0.55 value obtained in our best device (Table 1). Finally, the efficiency limit η_{max} under AM1.5 illumination is calculated as the product:

$$\eta_{max} = \frac{J_{sc} V_{oc} FF}{P_{inc}}$$

where P_{inc} is the incident power of 100 mW/cm^2 for AM1.5 illumination. Using the values reported above, we obtain η_{max} = 9% for nanotubes with large diameter of 1.2−1.7 nm, and η_{max} = 13% for nanotubes with small diameter of 0.75−1.2 nm. We remark that the alternative option of using FF = 0.85 and EQE = 0.85 (both of which have already been achieved in optimized organic solar cells, see ref 34) would lead to efficiency calculated values 10% higher than those reported here. In comparing these calculated values to the performance of the devices fabricated in this work, we note that while V_{oc} is near-optimal despite the limited efforts in our work to optimize this parameter, whereas J_{sc} is 7−10 times lower than the limit value of ~20 mA/cm^2. We believe that the main challenges toward significantly increasing J_{sc} lie in the fabrication of thicker active layers than shown here (only ~100 nm) and the use of materials with higher purity to minimize recombination.

It must be noted that the efficiency limits of 9−13% predicted here for nanocarbon-based PV exceed those predicted for polymer-solar cells based on PCBM acceptors, where $\eta_{max} \approx 11\%$ has been estimated[33] and practically achieved after a decade of intense research. The main reason for this is similarity that the optical gap of PCBM is similar to that of common polymer absorbers such as P3HT. However, the added benefit of using carbon as shown in this work is the superior photostability, indeed a critical feature for widespread applications of the solar cells. Research efforts similar to those responsible for the rapid efficiency increase of polymer-based solar cells should be undertaken for carbon-based devices, by identifying high-mobility and high purity semiconducting carbon materials, both in bulk and nanostructured forms, amenable to low cost mass-fabrication.

CONCLUSION

In summary, our results demonstrate that carbon-based PV active layers free of conjugated polymers or small molecules constitute a promising novel direction for photostable, efficient, solution processable, thin-film solar cells that are amenable to large-scale manufacturing. Candidate active layer materials are not limited to nanotubes and fullerenes as shown here, but rather span a vast array of suitable carbon compounds with yet untapped potential for thin-film solar cells. In combination with recently reported carbon-based transparent electrodes, carbon PV active layers could enable the development of efficient "all-carbon" solar cells.

METHODS

Preparation and Characterization of Carbon-Based Solar Cell Devices. We used two distinct samples of high purity s-SWCNT (IsoNanotube-S from NanoIntegris, 98% purity) with different diameters in the range of, respectively, 0.75−1.2 nm and 1.2−1.7 nm and lengths in the 300 nm to 5 μm range in both cases. The nanotube sample with d = 0.75−1.2 nm contained up to 50% of (6,5) nanotubes. Fullerene derivatives (6,6)-phenyl-C(X+1)-butyric acid methyl ester (PC_XBM), with X = 60 or 70 were purchased from Sigma Aldrich. Graphene oxide was prepared in-house by a modified Hummers method starting from graphite powder (Bay Carbon, SP-1). The as-synthesized GO was dispersed in dimethylformamide and sonicated for 20 min, and then reduced by heating in an oil bath at 150 °C for 1 h. The oxygen

concentration of rGO employed for device fabrication was determined to be in the range of ~10−20 atom % by Fourier transform infrared (FT-IR) and NMR spectroscopies. Carbon-based PV devices were prepared in a nitrogen glovebox and consisted of the following sequence of films and thicknesses: ITO/PEDOT:PSS(40 nm)/TFB (10 nm)/CPV (120 nm)/Al (100 nm), where (1) ITO is indium tin oxide (20 Ohm/Sq from Thin Film Devices), in the form of a 0.5 × 0.5 in^2 glass substrate with prepatterned ITO electrodes; (2) PEDOT:PSS is poly(3,4-ethylenedioxythiophene) poly(styrenesulfonate) (Clevios), a transparent hole conducting layer spun cast onto ITO; (3) TFB is poly[(9,9-dioctylfluorenyl-2,7-diyl)-co-(4,4′-(*N*-(4-s butylphenyl)) diphenylamine)] (American Dye Source), an electron blocking layer; (4) CPV is a blend of carbon nanomaterials including s-SWCNT, PCBM, and rGO with different compositions as shown in Table 1. Carbon nanomaterials were dissolved, sonicated, and filtered in 1,2-dichlorobenzene, spun cast at 600 rpm for 60 s, and allowed to solvent anneal overnight. The sonication was performed using a low-power benchtop sonicator for 30 min without heating. Such mild sonication conditions do not lead to formation of the ODCB polymer, as confirmed by high-resolution transmission electron microscopy. (5) Al metal was evaporated at a rate of 1 nm/s as the top contact layer. The final device area was defined by the overlap between the top and bottom electrodes. Current−voltage (*I*−*V*) characteristics of the devices were measured in a glovebox with a source-meter (Keithley 6487). The PV performance (power conversion efficiency and *I*−*V* curves) was measured under illumination from a 100 mW/cm^2, AM1.5 solar simulator. Over 10 devices of each kind reported in Table 1 were fabricated and tested, yielding a 5% standard deviation on the efficiency. Transmittance and absorbance spectra of the device active layer were measured with a Shimadzu UV−vis−NIR dual-beam spectrophotometer (UV-3600). External quantum efficiency (EQE) measurements were collected in a glovebox using a monochromator, chopped locked-in, and an NREL calibrated Ge detector (Newport). Surface morphology of the devices was investigated using an atomic force microscope (Digital Instruments Dimension 3000).

Computational Design of Carbon Interfaces. Density functional theory calculations were performed using the VASP[35] and Quantum Espresso codes[36] with the Perdew−Burke−Ernzerhof exchange-correlation functional.[37] A kinetic energy cutoff of 35 Ry was used for the plane-wave basis set and of 200 Ry for the charge density, and all structures were relaxed to less than 50 meV/A in their residual atomic forces. For the s-SWCNT/PC_{60}BM interfaces, ultrasoft pseudopotentials[38] were used to describe the core electrons. An orthorhombic unit cell with 10 A vacuum in the nonperiodic directions was employed. Between 1 and 4 SWCNT repeat units (depending on the nanotube chirality) were used with a Monkhorst-Pack *k*-grid of 1 × 1 × n_z, where n_z values up to 20 were used for a converged number of *k*-points in the nanotube axis direction. The PCBM was placed at a van der Waals distance of ~3.3 A next to the nanotube and relaxed to eliminate residual forces; the final calculations were carried out on such combined PCBM/s-SWCNT systems with up to ~500 valence electrons. The HOMO and LUMO level offsets were computed as differences in the peaks of the projected density of states obtained for the two molecules in the combined system. For electronic structure and workfunction calculations on rGO, and for the determination of Schottky barriers (SB) at rGO/PCBM and rGO/s-SWCNT interfaces, projector augmented−wave (PAW) pseudopotentials[39] were employed as implemented in the VASP code.[35] Representative rGO structures were assumed to consist of epoxy, hydroxyl, carbonyl, and ether groups, and were generated by randomly placing functional groups in different proportions on a square cut of the graphene sheet (180 C atoms), similar to the method used in ref 40. The structures were first relaxed using the MMFF94 force field and further relaxed in DFT. The oxygen content was varied between 10−20 atom % to consider structures with the same O concentration range as in the experiment. For the rGO/PCBM and rGO/s-SWCNT interface calculations, the PCBM (or s-SWCNT) was placed at a van der Waals distance of 3.5−4.0 A from the graphene basal plane depending on the O content of the rGO structure. Only the p-type Schottky barrier (E_p) at the interface was calculated directly using DFT with a method detailed in ref 41. The n-type Schottky barrier (E_n) in the case of rGO/PCBM was obtained using the relation, $E_n = E_g - E_p$ where E_g is the experimental electronic gap of PCBM (~2 eV, see ref 27), and where we used the fact that the sum of the n-type and p-type barriers is numerically equal to the semiconductor energy gap. No assumptions were made about the position of the Fermi energy, and chemical doping was not assumed. For each concentration, the SB was obtained as the average value over three different PCBM (or s-SWCNT) positions in the simulation cell, with a small standard deviation of ~0.1 eV.

Conflict of Interest: The authors declare no competing financial interests.

Acknowledgment. M.B. acknowledges funding from Intel through the Intel Ph.D. Fellowship. N.F. and J.C.G. are grateful to the MITEI seed program for financial support. M.B., P.V.K., and J.C.G., wish to thank NERSC and Teragrid for providing computational resources. S.R. thanks the University of Kansas for its startup financial support, and acknowledges funding from a Department of Energy award (DESC0005448).

Supporting Information Available: Computed Schottky barriers; EQE for small diameter nanotube solar cells; additional photodegradation data. This material is available free of charge *via* the Internet at http://pubs.acs.org.

REFERENCES AND NOTES

1. SunShot Vision Study, Chapter 1 (2012). http://www1.eere.energy.gov/solar/sunshot/vision_study.html. See also *Nat. Mater.* **2012**, *11*, 178−179.
2. Ginley, D.; Green, M. A.; Collins, R. Solar Energy Conversion Toward 1 Terawatt. *MRS Bull.* **2008**, *33*, 355–364.
3. Shockley, W; Queisser, H. J. Detailed Balance Limit of Efficiency of p−n Junction Solar Cells. *J. Appl. Phys.* **1961**, *32*, 510–519.
4. Mayer, A. C.; Scully, S. R.; Hardin, B. E.; Rowell, M. W.; McGehee, M. D. Polymer-Based Solar Cells. *Mater. Today* **2007**, *10*, 28–33.
5. Moule', A. J. Power from Plastic. *Curr. Opin. Solid State Mater. Sci.* **2010**, *14*, 123–130.
6. Sun, Y.; Welch, G. C.; Leong, W. L.; Takacs, C. J.; Bazan, G. C.; Heeger, A. J. Solution-Processed Small-Molecule Solar Cells with 6.7% Efficiency. *Nat. Mater.* **2011**, *11*, 44–48.
7. Koleilat, G. I.; Levina, L.; Shukla, H.; Myrskog, S. H.; Hinds, S.; Pattantyus-Abraham, A. G.; Sargent, E. H. Efficient, Stable Infrared Photovoltaics Based on Solution-Cast Colloidal Quantum Dots. *ACS Nano* **2008**, *2*, 833–840.
8. Zhu, H.; Wei, J.; Wang, K.; Wu, D. Applications of Carbon Materials in Photovoltaic Solar Cells. *Sol. Energy Mater. Sol. Cells* **2009**, *93*, 1461–1470.
9. Cox, P. A. *The Elements: Their Origin, Abundance, and Distribution*; Oxford University Press: New York, NY, 1989. See also http://www.webelements.com/periodicity/abundance_crust/
10. Iijima, S. Helical Microtubules of Graphitic Carbon. *Nature* **1991**, *354*, 56–58.
11. Saito, R.; Dresselhaus, G.; Dresselhaus, M. S. *Physical Properties of Carbon Nanotubes*; Imperial: London, 1998.
12. Kroto, H. W.; Heath, J. R.; O'Brien, S. C.; Curl, R. F.; Smalley, R. E. C60: Buckminsterfullerene. *Nature* **1985**, *318*, 162–163.
13. Geim, A. K.; Novoselov, K. S. The Rise of Graphene. *Nat. Mater.* **2007**, *6*, 183–191.
14. Geim, A. Graphene: Status and Prospects. *Science* **2009**, *324*, 1530–1534.
15. Avouris, P.; Martel, R. Progress in Carbon Nanotube Electronics and Photonics. *MRS Bull.* **2010**, *35*, 306–313.
16. Ren, S.; Bernardi, M.; Lunt, R. R.; Bulovic, V.; Grossman, J. C.; Gradecak, S. Toward Efficient Carbon Nanotube/P3HT Solar Cells: Active Layer Morphology, Electrical and Optical Properties. *Nano Lett.* **2011**, *11*, 5316–5321.
17. Bindl, D. J.; Safron, N. S.; Arnold, M. S. Dissociating Excitons Photogenerated in Semiconducting Carbon Nanotubes at

Polymeric Photovoltaic Heterojunction Interfaces. *ACS Nano* **2010**, *4*, 5657–5664.
18. Bindl, D. J.; Wu, M.-Y.; Prehn, F. C.; Arnold, M. S. Efficiently Harvesting Excitons from Electronic Type-Controlled Semiconducting Carbon Nanotubes Films. *Nano Lett.* **2011**, *11*, 455–460.
19. Jain, R. M.; Howden, R.; Tvrdy, K.; Shimizu, S.; Hilmer, A. J.; McNicholas, T. P.; Gleason, K. K.; Strano, M. S. Polymer-free Near-Infrared Photovoltaics with Single Chirality (6,5) Semiconducting Carbon Nanotube Active Layers. *Adv. Mater.* **2012**, *24*, 4436–4439.
20. Tung, V. C.; Huang, J.-H.; Tevis, I.; Kim, F.; Kim, J.; Chu, C.-W.; Stupp, S. I.; Huang, J. Surfactant-Free Water-Processable Photoconductive All-Carbon Composite. *J. Am. Chem. Soc.* **2011**, *133*, 4940–4947.
21. Tung, V. C.; Huang, J.-H.; Kim, J.; Smith, A. J.; Chu, C.-W.; Huang, J. Towards Solution Processed All-Carbon Solar Cells: A Perspective. *Energy Environ. Sci.* **2012**, *5*, 7810–7818.
22. Loh, K. P.; Bao, Q.; Eda, G.; Chhowalla, M. Graphene Oxide as a Chemically Tunable Platform for Optical Applications. *Nat. Chem.* **2010**, *2*, 1015–1024.
23. Wienk, M. M.; Kroon, J. M.; Verhees, W. J. H.; Knol, J.; Hummelen, J. C.; van Hal, P. A.; Janssen, R. A. J. Efficient Methano[70]fullerene/MDMO–PPV Bulk Heterojunction Photovoltaic Cells. *Angew. Chem., Int. Ed.* **2003**, *42*, 3371–3375.
24. Kymakis, E.; Amaratunga, G. A. J. In *Organic Photovoltaics*; Sun, S.-S., Sariciftci, N. S., Eds.; CRC Press: Boca Raton, FL, 2005.
25. Martin, R. *Electronic Structure: Basic Theory and Practical Methods*; Cambridge University Press: Cambridge, UK, 2004.
26. We remark that the band alignment calculations presented here are based on DFT with semilocal exchange correlation functional. While this method can yield accurate valence band offsets between sp-bonded materials interacting by van der Waals forces (as studied here), the accuracy of the conduction band offsets is a consequence of a cancellation of the error on the energy gaps of the two materials composing the interface. For the interfaces studied here with up to 500 valence electrons more accurate calculations with nonlocal functionals (*e.g.*, hybrid DFT or GW self-energy methods) are however unfeasible at present. Nonetheless the error cancellation leads to qualitatively correct trends and band offsets predictions as verified experimentally in Figure 2.
27. Akaike, K.; Kanai, K.; Yoshida, H.; Tsutsumi, J.; Nishi, T.; Sato, N.; Ouchi, Y.; Seki, K. Ultraviolet Photoelectron Spectroscopy and Inverse Photoemission Spectroscopy of [6,6]-Phenyl-C_{61}-Butyric Acid Methyl Ester in Gas and Solid Phases. *J. Appl. Phys.* **2008**, *104*, 023710.
28. Hayashi, H.; Lightcap, I. V.; Tsujimoto, M.; Takano, M.; Umeyama, T.; Kamat, P. V.; Imahori, H. Electron Transfer Cascade by Organic/Inorganic Ternary Composites of Porphyrin, Zinc Oxide Nanoparticles, and Reduced Graphene Oxide on a Thin Oxide Electrode that Exhibits Efficient Photocurrent Generation. *J. Am. Chem. Soc.* **2011**, *133*, 7684–7687.
29. Peters, C. H.; Sachs-Quintana, I. T.; Mateker, W. R.; Huemueller, T.; Rivnay, J.; Noriega, R.; Beiley, Z. M.; Hoke, E. T.; Salleo, A.; McGehee, M. D. The Mechanism of Burn-in Loss in a High Efficiency Polymer Solar Cell. *Adv. Mater.* **2012**, *24*, 663–668.
30. Reese, M. O.; Nardes, A. M.; Rupert, B. L.; Larsen, R. E.; Olson, D. C.; Lloyd, M. T.; Shaheen, S. E.; Ginley, D. S.; Rumbles, G.; Kopidakis, N. Photoinduced Degradation of Polymer and Polymer-Fullerene Active Layers: Experiment and Theory. *Adv. Funct. Mater.* **2010**, *20*, 3476–3483.
31. Wurfel, P. *Physics of Solar Cells*, 2nd ed.; Wiley-VCH: Weinheim, Germany, 2009.
32. The AM1.5G spectrum was taken from the NREL web-site: http://rredc.nrel.gov/solar/spectra/am1.5 and integrated with the trapezoid rule (accessed July 20, 2012).
33. Scharber, M. C.; Muhlbacher, D.; Koppe, M.; Denk, P.; Waldauf, C.; Heeger, A. J.; Brabec, C. J. Design Rules for Donors in Bulk-Heterojunction Solar Cells—Towards 10% Energy Conversion Efficiency. *Adv. Mater.* **2006**, *18*, 789–794.
34. Lunt, R. R.; Osedach, T. O.; Brown, P. R.; Rowehl, J. A.; Bulovic, V. Practical Roadmap and Limits to Nanostructured Photovoltaics. *Adv. Mater.* **2011**, *23*, 5712–5726.
35. Kresse, G.; Furthmüller, J. Efficient Iterative Schemes for *ab Initio* Total-Energy Calculations Using a Plane-Wave Basis Set. *Phys. Rev. B* **1996**, *54*, 11169–11186.
36. Giannozzi, P.; Baroni, S.; Bonini, N.; Calandra, M.; Car, R.; Cavazzoni, C.; Ceresoli, D.; Chiarotti, G. L.; Cococcioni, M.; Dabo, I.; *et al.* QUANTUM ESPRESSO: a Modular and Open–Source Software Project for Quantum Simulations of Materials. *J. Phys.: Condens. Matter* **2009**, *21*, 395502.
37. Perdew, J. P.; Burke, K.; Ernzerhof, M. Generalized Gradient Approximation Made Simple. *Phys. Rev. Lett.* **1996**, *77*, 3865–3868.
38. Vanderbilt, D. Soft Self-Consistent Pseudopotentials in a Generalized Eigenvalue Formalism. *Phys. Rev. B* **1990**, *41*, 7892–7895.
39. Blochl, P. E. Projector Augmented–Wave Method. *Phys. Rev. B* **1994**, *50*, 17953–17979.
40. Paci, J. T.; Belytschko, T.; Schatz, G. C. Computational Studies of the Structure, Behavior upon Heating, and Mechanical Properties of Graphite Oxide. *J Phys. Chem. C* **2007**, *111*, 18099–18111.
41. Shan, B.; Cho, K. *Ab–Initio* Study of Schottky Barriers at Metal–Nanotube Contacts. *Phys. Rev. B* **2004**, *70*, 233405.